

Lawrence Berkeley National Laboratory

LBL Publications

Title

Theoretical and Experimental Study on the Optoelectronic Properties of Nb₃O₇(OH) and Nb₂O₅ Photoelectrodes

Permalink

<https://escholarship.org/uc/item/3hx2q287>

Journal

The Journal of Physical Chemistry C, 120(41)

ISSN

1932-7447

Authors

Khan, Wilayat
Betzler, Sophia B
Šipr, Ondřej
[et al.](#)

Publication Date

2016-10-20

DOI

10.1021/acs.jpcc.6b06391

Peer reviewed

Theoretical and Experimental Study on the Optoelectronic Properties of $\text{Nb}_3\text{O}_7(\text{OH})$ and Nb_2O_5 Photoelectrodes

Wilayat Khan,[†] Sophia B. Betzler,[‡] Ondřej Šipr,^{†,¶} Jim Ciston,^{||} Peter Blaha,[⊥] Christina Scheu,[#] and Jan Minar^{*,†,‡}

[†]New Technologies-Research Center, University of West Bohemia, Univerzitní 8, 306 14 Plzeň, Czech Republic

[‡]Department of Chemistry and Center for NanoScience, LMU Munich, Butenandtstraße 11, 81377 Munich, Germany

[¶]Institute of Physics of the ASCR v. v. i., Cukrovarnická 10, CZ-162 53 Prague, Czech Republic

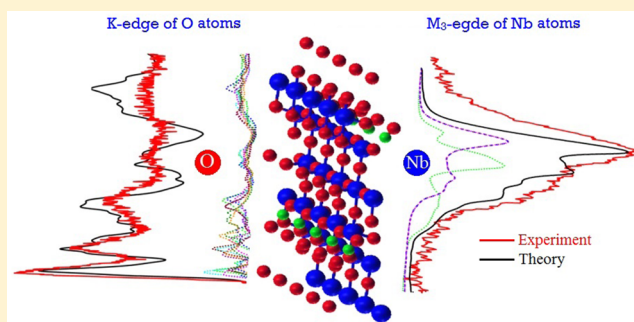
^{||}National Center for Electron Microscopy, Molecular Foundry, Lawrence Berkeley National Laboratory, 1 Cyclotron Road, Berkeley, California 94720 United States

[⊥]Institute of Materials Chemistry, Vienna University of Technology, Getreidemarkt 9/165-TC, A-1060 Vienna, Austria

[#]Max-Planck-Institut für Eisenforschung GmbH, Max-Planck-Straße 1, Düsseldorf, Germany

Supporting Information

ABSTRACT: $\text{Nb}_3\text{O}_7(\text{OH})$ and Nb_2O_5 nanostructures are promising alternative materials to conventionally used oxides, e.g. TiO_2 , in the field of photoelectrodes in dye-sensitized solar cells and photoelectrochemical cells. Despite this important future application, some of their central electronic properties such as the density of states, band gap, and dielectric function are not well understood. In this work, we present combined theoretical and experimental studies on $\text{Nb}_3\text{O}_7(\text{OH})$ and $\text{H-Nb}_2\text{O}_5$ to elucidate their spectroscopic, electronic, and transport properties. The theoretical results were obtained within the framework of density functional theory based on the full potential linearized augmented plane wave method. In particular, we show that the position of the H atom in $\text{Nb}_3\text{O}_7(\text{OH})$ has an important effect on its electronic properties. To verify theoretical predictions, we measured electron energy-loss spectra (EELS) in the low loss region, as well as, the O–K and Nb–M₃ element-specific edges. These results are compared with corresponding theoretical EELS calculations and are discussed in detail. In addition, our calculations of thermoelectric conductivity show that $\text{Nb}_3\text{O}_7(\text{OH})$ has more suitable optoelectronic and transport properties for photochemical application than the calcined $\text{H-Nb}_2\text{O}_5$ phase.



I. INTRODUCTION

The consumption of fossil fuel stocks presents our society with a new challenge and forces the research for alternatives. Efficient harvesting of the power of the sun with solar cells would suffice to cover the worldwide energy consumption. To balance out fluctuations in the energy production novel storage technologies need to be developed simultaneously and in this regard hydrogen is intensively discussed as a very promising material for energy storage. Dye-sensitized solar cells (DSSC) and photocatalysis both apply semiconductors to generate charges which are either separated to produce current or used up for chemical reactions (e.g., the splitting of water to produce hydrogen gas). The solar energy is absorbed by the semiconductor whereby an electron is excited from the valence to the conduction band leading to electron–hole pairs.^{1,2} The band gap size and energy position of the conduction and valence band edges of the semiconductor are crucial for the performance of a semiconductor in photochemistry as they determine the portion of the solar spectrum absorbable by the semiconductor, the potential of the electron–hole pair and the

band alignment of the device.^{3,4} Theoretical studies calculated the band edge energies of a high variety of oxides,^{5–8} predicting their applicability as photocatalyst or electrode material. Subsequent to their separation, the generated charges need to diffuse to the surface of the semiconductor. This process is endangered by charge recombination: a major loss mechanism leading to reduced quantum yields. Consequently, both the charge transport properties and the energy position of the band gap of a material have to be taken into account at evaluating its applicability as photocatalyst. Still, the ideal material system was not yet discovered⁹ and research needs to go beyond established material systems. This study focuses on the prediction of material properties of a material class which was very recently discovered as new material with attractive properties for photochemistry: Several experimental studies show the applicability of $\text{Nb}_3\text{O}_7(\text{OH})$ ^{10,12–14,16} and

Received: June 24, 2016

Revised: September 16, 2016

Published: September 16, 2016

Nb_2O_5 ^{10,11,17–23} as photocatalyst and electrode material in DSSCs. $\text{Nb}_3\text{O}_7(\text{OH})$ can be transformed into monoclinic $\text{H-Nb}_2\text{O}_5$ by calcination.^{10,24} The changes of the material properties which go along with this phase-transformation will be investigated on a theoretical basis in this study.

Density functional theory (DFT) is widely used for ground states calculations in physics, chemistry, and material science.^{25,26} DFT is very useful to predict the exact ground state properties, but in particular electronic properties of semiconductors related to excited states such as, e.g., the size of the band gap, strongly depend on the choice of the exchange correlation functional. Recently, Zhang et al.¹⁰ studied structural properties of $\text{Nb}_3\text{O}_7(\text{OH})$ and Nb_2O_5 oxides by means of generalized gradient approximation (GGA),²⁷ which is in general well suited to obtain accurate structural parameters.²⁸ On the basis of this functional, Zhang et al. discussed in detail the position of H atoms in the hydroxide $\text{Nb}_3\text{O}_7(\text{OH})$. However, the calculations of electronic structure properties of these materials such as the density of states, band gap and dielectric function are not well understood. As a first step of our study we have tested various exchange-correlation functionals such as, i.e., the local density approximation (LDA),²⁹ the GGA,²⁷ Engel Vosko (EVGGA),³⁰ and Tran and Blaha modified Becke Johnson (TB-mBJ).³¹ Here we show, that within the TB-mBJ functional predicted electronic and optical properties of $\text{Nb}_3\text{O}_7(\text{OH})$ and Nb_2O_5 agree very well with measured low-loss spectra, as well as the near edge fine structure of the O–K and Nb– M_3 edges of $\text{Nb}_3\text{O}_7(\text{OH})$. This gives new insights into the structure of the edge. The electronic structure furthermore forms the basis for the determination of the thermoelectric conductivity of the two compounds with the BoltzTraP³² code.

II. COMPUTATIONAL AND EXPERIMENTAL METHODOLOGY

II.A. Calculation Details. All density functional theory based calculations were performed using the linearized augmented plane wave + local orbitals (LAPW+lo) method as implemented in the WIEN2k code.³³ The muffin tin radii R_{MT} for $\text{Nb}_3\text{O}_7(\text{OH})$ were set to 1.8, 1.3, and 0.55 bohr for the niobium, oxygen and hydrogen atoms, respectively. The muffin tin radii for monoclinic $\text{H-Nb}_2\text{O}_5$ were set to 1.74 bohr for niobium atoms and 1.58 bohr for oxygen atoms. The wave functions in the atomic spheres were expanded up to an angular momentum of $l = 10$. The plane wave cutoff in the interstitial region was set so that $R_{\text{MT}} \times K_{\text{MAX}} = 7$ for Nb_2O_5 and 3 for $\text{Nb}_3\text{O}_7(\text{OH})$, respectively. and was validated by convergence of the forces on the atoms. To obtain the electronic structure as well as optical properties we used a k -point mesh of $16 \times 16 \times 15$ for $\text{Nb}_3\text{O}_7(\text{OH})$ and $3 \times 18 \times 4$ for Nb_2O_5 .

The structural relaxations were done using the GGA²⁷ functional. Since it is well-known than local exchange correlation functionals underestimate band gaps, the electronic structure calculations were performed using the TB-mBJ approach. This functional usually predicts band gaps with higher accuracy³¹ than GGA. However, we also performed all calculations with GGA and with LDA functionals so that a detailed comparison of the results obtained using different exchange-correlation functionals with the experiment is possible. This comparison demonstrated that the TB-mBJ approach is suitable for the Nb oxides studied here (see section III.D, below).

The linear optical properties of $\text{Nb}_3\text{O}_7(\text{OH})$ and $\text{H-Nb}_2\text{O}_5$ were derived from the OPTIC program³⁴ included in the WIEN2k simulation package. The imaginary part of the dielectric tensor (ϵ_2) was calculated according to ref 35. The real part of the dielectric function (ϵ_1) is derived from the Kramers–Kronig relation.³⁶ Both the optical conductivity $\sigma(\omega) = \frac{\omega}{2\pi}\epsilon_2(\omega)$ and the energy loss function $L(\omega) = \frac{\epsilon_2(\omega)}{[\epsilon_1(\omega)]^2 + [\epsilon_2(\omega)]^2}$ can be calculated directly from $\epsilon_1(\omega)$ and $\epsilon_2(\omega)$.³⁷

Core loss electron energy-loss spectra of Nb– M_3 and O–K edges were calculated with the X-ray absorption module of the WIEN2k code. The application of Fermi's golden rule is possible for the used experimental scattering geometry as the dipole approximation is fairly valid.³⁸ We had to account for the core hole to achieve a satisfying agreement between theoretical and experimental core loss data at the O–K and Nb– M_3 edge. This was done using the static core hole approach. One of the relevant core electrons was removed, the number of valence electrons was increased by one and a self-consistent calculation was done so that the electrons adjust to the presence of the core hole. This calculation was done for every nonequivalent oxygen and niobium atom in the unit cell using a $2 \times 2 \times 1$ supercell.

The BoltzTraP code³² was used to calculate the electrical conductivity under constant relaxation time τ .^{39,40} These calculations are based on the Boltzmann transport theory and necessary information about the band dispersion is obtained by corresponding DFT calculation.

II.B. Experimental Details. In addition to the theoretical calculations, we performed electron energy-loss spectroscopy (EELS) measurements in a transmission electron microscope (TEM). The $\text{Nb}_3\text{O}_7(\text{OH})$ sample was synthesized according to the procedure described by Betzler et al.¹⁴ Monoclinic $\text{H-Nb}_2\text{O}_5$ was obtained by calcination of $\text{Nb}_3\text{O}_7(\text{OH})$ at 850 °C.¹⁵ Low loss data were acquired to get experimental information about the optical response of the samples. In addition core loss data were recorded to investigate the coordination and bonding characteristic of the crystal lattices. The low loss spectra were detected using a double corrected FEI-TEAM 0.5 microscope operated at 300 kV. An energy resolution of 0.15 to 0.18 eV (determined by the full width at half-maximum of the zero-loss peak) was achieved using a monochromator and a spectrometer entrance aperture of 1 mm under parallel illumination of the sample (convergence angle below 0.2 mrad). The linear fit method⁴¹ enables the determination of the band gap of materials from the low-loss region (energy losses between 0 and 50 eV). In addition optical extinction data were detected for a spectral region of 250 to 1200 nm. The Tauc method⁴² was applied to determine the band gap based on optical data and it was used compared to the band gaps measured by EELS. The element specific edges were measured using a Zeiss Libra microscope operated at 200 kV with parallel illumination (convergence angle about 0.2 mrad). An energy resolution of 0.3–0.4 eV was achieved for the determination of the O–K and Nb– M_3 edges using a monochromator and a collection angle of 17 mrad. The spectra were detected with a dispersion of 0.07 eV/channel.

III. RESULTS AND DISCUSSION

III.A. Structural Optimization. We considered three systems in our study: monoclinic $\text{H-Nb}_2\text{O}_5$, orthorhombic

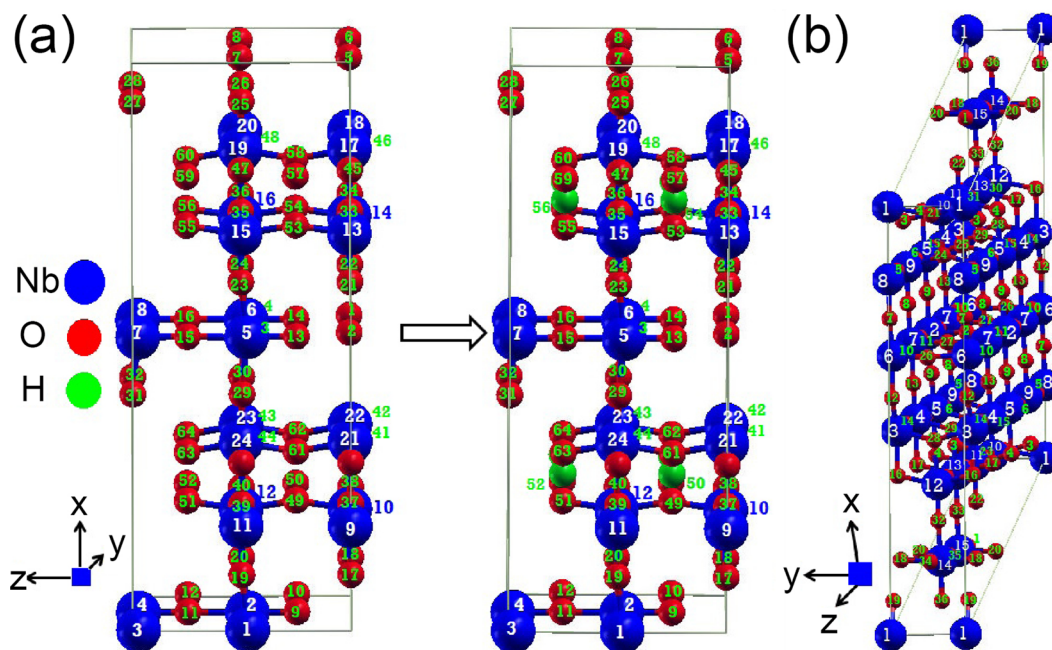


Figure 1. Schematic representation of the crystal structures of the artificial reference compound Nb_3O_8 (left, a) and $\text{Nb}_3\text{O}_7(\text{OH})$ (right, a) and monoclinic $\text{H-Nb}_2\text{O}_5$ (b). Black, red, and green spheres represent Nb, O, and H atoms, respectively.

$\text{Nb}_3\text{O}_7(\text{OH})$ and an auxiliary Nb_3O_8 system. Please note that all relaxed structures used in this manuscript can be found as crystallographic cif files in the [Supporting Information](#).

$\text{Nb}_3\text{O}_7(\text{OH})$ and Nb_3O_8 . $\text{Nb}_3\text{O}_7(\text{OH})$ has an orthorhombic structure isomorphous with $\text{Nb}_3\text{O}_7\text{F}$, which crystallizes in $Cmcm$ (number 65) space group.^{43,44} The experimental unit cell parameters are $a = 20.74$, $b = 3.823$, $c = 3.936$ Å. It is well-known that it is very difficult to find the exact position of H atoms by means of X-ray diffraction. Therefore, theoretical studies are important here. Zhang et al.¹⁰ based their DFT calculations on a suggested position for the H atom: Here the H atom is attached to an oxygen atom O(8) between two Nb(3) sites (Nb(2) and (3) are situated in edge-sharing oxygen octahedra, while Nb(1) sits in a corner-sharing one). We used their structural model as starting point for our structure relaxation. The structure of $\text{Nb}_3\text{O}_7(\text{OH})$ which we obtained is quite similar to the structure of Zhang et al.;¹⁰ a perspective diagram is shown [Figure 1a](#). The largest difference between our results and the structure found by Zhang et al.¹⁰ concern the region close to the OH group: the O–H distance increased by 0.359 Å (1.07 Å in relaxed, –1.429 Å in unrelaxed structure model) and the Nb–O distance by 0.053 Å (2.030 Å in relaxed, –1.977 Å in unrelaxed state).

To study the bare effects of the hydrogen atom on the electronic structure, optoelectronic and transport properties, we also performed calculations for an artificial Nb_3O_8 reference compound. Nb_3O_8 is not known experimentally and was defined by removing the H atom from the crystal lattice of $\text{Nb}_3\text{O}_7(\text{OH})$ while leaving all structural parameters as in the original $\text{Nb}_3\text{O}_7(\text{OH})$ compound.

$\text{H-Nb}_2\text{O}_5$. Nb_2O_5 exhibits more than 15 different polymorphs.⁴⁵ Monoclinic $\text{H-Nb}_2\text{O}_5$ is the thermodynamic stable polymorph which forms after calcination of $\text{Nb}_3\text{O}_7(\text{OH})$ at 500 °C.¹⁰ Its crystal structure was determined experimentally by Gatehouse et al.⁴⁶ and Kato.⁴⁷ It crystallizes in the space group $P2/m$ (number 10), with lattice parameters $a = 21.153$, $b = 3.823$ and $c = 19.356$ Å and $\gamma = 119.5^\circ$. There are 15

inequivalent Nb sites in this structure, one of them corresponds to a disordered position: the corresponding Nb atom occupies the $2i$ Wyckoff positions, each of the statistical displacements of $y = \pm 0.2285$ is occupied with concentration of 0.5. We ignored this partial fractional occupancy by occupying instead Wyckoff position $1a$ [at (0.0, 0.0, 0.0)] with occupation 1.0. This geometry was then optimized by minimizing the forces exerted on the atoms, keeping the overall unit cell parameters constant. The relaxed structure of $\text{H-Nb}_2\text{O}_5$ we thereby obtained is shown in [Figure 1b](#). The changes with respect to the original experimental structure^{46,47} are generally small: the bond lengths typically changed by 0.001–0.050 Å, only in one case the Nb–Nb bond length increased by 0.20 Å and in one case the O–O bond length increase by 0.11 Å. The largest change of course concerns the Nb atom that was transferred from the $2i$ site to the $1a$ site. In the relaxed structure all Nb atoms are coordinated octahedrally by oxygen.

III.B. Electronic Band Structures. The response range of a semiconductor in the visible light regime is determined by the size of its band gap and its band structure, while its ability to successfully participate at the chemical reaction depends on the energetic position of the gap. The electronic band dispersions of orthorhombic Nb_3O_8 and $\text{Nb}_3\text{O}_7(\text{OH})$ as well as monoclinic $\text{H-Nb}_2\text{O}_5$ are plotted in [Figure 2a–c](#) along the high symmetry lines inside the irreducible Brillouin zone (IBZ). The band structure calculation of all three compounds was performed using the TB-mBJ³¹ approach. It is very difficult to predict the accurate position of the H atom in the crystal lattice of $\text{Nb}_3\text{O}_7(\text{OH})$ from both experiment as well as theory. As described above we model the H positions following Zhang et al.¹⁰ The energetically lowest position for H atom can be found in the octahedra of Nb(3) atom as it is shown in [Figure 1a](#). The use of the suggested relaxed crystal structure shows semiconducting properties with an indirect band gap for $\text{Nb}_3\text{O}_7(\text{OH})$ and a fundamental band gap of 1.70 eV. The comparison with the reference compound Nb_3O_8 exhibits that the presence of hydrogen in the crystal lattice shifts the Fermi

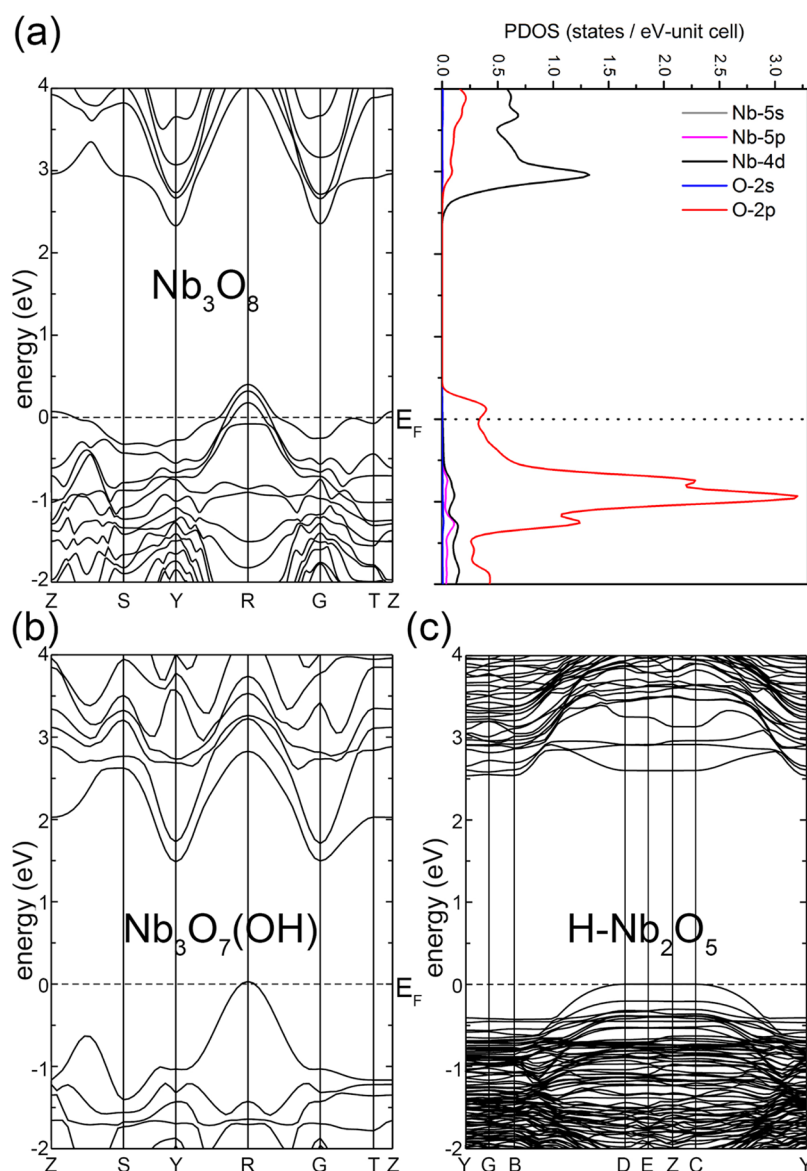


Figure 2. Calculated band structures of Nb_3O_8 (left side, a), $\text{Nb}_3\text{O}_7(\text{OH})$ (b), and monoclinic $\text{H-Nb}_2\text{O}_5$ (c). In addition the density of states is given for Nb_3O_8 on the right side of part a.

energy to the top of the valence bands resulting in a change from metallic (Nb_3O_8) to semiconducting ($\text{Nb}_3\text{O}_7(\text{OH})$) properties. In addition the uppermost valence band shows a much larger dispersion for $\text{Nb}_3\text{O}_7(\text{OH})$ than Nb_3O_8 and the conduction bands are shifted to lower energies by 0.5 eV in $\text{Nb}_3\text{O}_7(\text{OH})$. Other than these changes of the band structure due to the H atom are small (Figure 2a,b).

Like $\text{Nb}_3\text{O}_7(\text{OH})$ monoclinic $\text{H-Nb}_2\text{O}_5$ is also an indirect band gap semiconductor with a larger fundamental band gap of 2.56 eV (Figure 2). The valence band maximum (VBM) and conduction band minimum (CBM) occur at R and Y symmetry points in $\text{Nb}_3\text{O}_7(\text{OH})$ while they appear at D, E, Z, C, and B symmetry points of the IBZ in $\text{H-Nb}_2\text{O}_5$. Indirect transitions need a momentum transfer supplied by phonons to realize k -conservation. The calculated findings for the band gaps are summarized in Table 1. In addition experimentally determined values are given which were obtained using both absorption spectroscopy and electron energy-loss spectroscopy. Optical spectroscopy yields a band gap of 3.1 eV for both compounds, while a slightly larger band gap of 3.2 eV is determined for $\text{H-Nb}_2\text{O}_5$

Table 1. Band gaps of $\text{Nb}_3\text{O}_7(\text{OH})$ and Nb_2O_5 determined experimentally and from calculation (in [eV])

	$\text{Nb}_3\text{O}_7(\text{OH})$	monoclinic $\text{H-Nb}_2\text{O}_5$
	Experimental Band Gap	
optical	3.09 (± 0.05)	3.07 (± 0.05)
EELS	3.1 (± 0.1)	3.2 (± 0.1)
	Theoretical Band Gap	
fundamental	1.70	2.56
optical	3.1	3.0

Nb_2O_5 from EEL spectra. This compares well with the calculated optical band gaps of the two compounds which were found to be 3.1 eV for $\text{Nb}_3\text{O}_7(\text{OH})$ and 3.0 eV for $\text{H-Nb}_2\text{O}_5$. The band gaps of the two niobium oxide phases are similar to TiO_2 ⁴⁸ and allow the absorption of light from the UV region ($\lambda < 390$ nm) of the solar spectrum.

The partial density of states (PDOS) reveal deeper insights into the band structure of $\text{Nb}_3\text{O}_7(\text{OH})$ and $\text{H-Nb}_2\text{O}_5$ (Figure 3a,b). The partial DOS confirms that the top of the valence

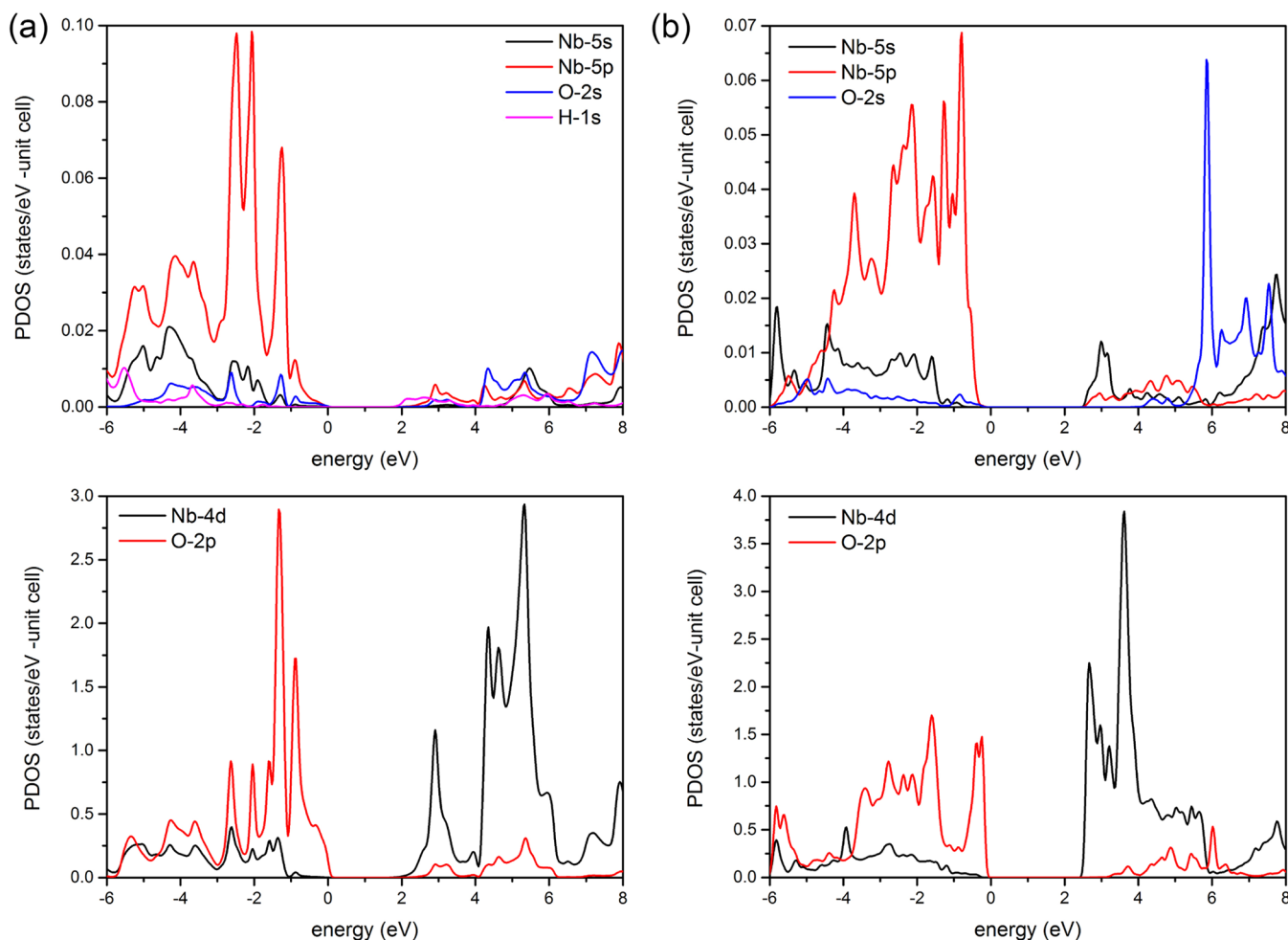


Figure 3. Partial density of states were calculated using the TB-mBJ approach: PDOS of Nb, O, and H atoms (a) for $\text{Nb}_3\text{O}_7(\text{OH})$ and (b) for monoclinic $\text{H-Nb}_2\text{O}_5$. Solid (black, red, blue, and green) lines represent s, p, and d states, respectively. The Fermi level (E_F) is set to zero.

bands of both compounds primarily originate from the O-2p orbitals, and the bottom of the conduction band mainly from Nb-4d orbitals with a negligible contribution of H-1s orbitals. The valence band of both $\text{Nb}_3\text{O}_7(\text{OH})$ and $\text{H-Nb}_2\text{O}_5$ is divided into two distinct regions: The energy region at -6.0 eV to ~ -4.0 eV is dominated equally by the 4d/2p orbitals of Nb and O atoms, while small contributions of Nb-5s/5p orbitals and H-1s orbital are also observed. A strong overlap is observed for the O-2p and Nb-4d orbitals (below 6.0 eV) and the oxygen 2s orbitals with the 5s orbitals of Nb atoms also show strong interplay at 5.5 eV. The second energy region at -4.0 to 0.0 eV is mainly assigned to O-2p but the Nb-4d orbitals contribute significantly less along with minor participation of 2s/5s/5p/1s orbitals of O/Nb/H atoms. The 2s/5s orbitals of O/Nb atoms (from -3.7 to ~ 0.0 eV) and the 1s/2s orbitals of H/O atoms of $\text{Nb}_3\text{O}_7(\text{OH})$ present strong interactions with each other at -2.2 eV, while the 2s/5s of O/Nb atoms (from -1.30 to 0.0 eV) in Nb_2O_5 only partially interact. The H-1s orbitals are more than -3.0 eV deeper in energy than the VBM since the H atom is coordinated solely by one O atom leading to negligible hybridization over all other atoms. The bands above the Fermi level at energy 2.34 eV ($\text{Nb}_3\text{O}_7(\text{OH})$) and 2.56 eV (Nb_2O_5) ~ 4.0 eV are robustly assigned to Nb-4d orbitals mixing with small contributions of s/p orbitals of O/Nb atoms. The region beyond 4.0 eV is still mainly composed of Nb-4d orbitals

combined with O-2p orbitals and minor participation of the remaining orbitals of Nb/O/H atoms.

From the above discussion it becomes clear that the O-2p (VBM) and Nb-4d (CBM) orbitals are predominately responsible for optical excitations in $\text{Nb}_3\text{O}_7(\text{OH})$ and $\text{H-Nb}_2\text{O}_5$. Furthermore, the investigations show that doping with H-1s causes a shifting of all peaks at the VBM toward lower regions as well as a broadening of these peaks (Figure 3a,b/2).

III.C. Optical Properties. It is known that semiconductors play an important role in the field of optoelectronic devices where the band gap defines the threshold energy of electromagnetic radiation and differentiates between transparency and absorbing region. The optical properties of $\text{Nb}_3\text{O}_7(\text{OH})$ and $\text{H-Nb}_2\text{O}_5$ were calculated by linear response formalism and the complex dielectric function (namely $\epsilon_1(\omega)$ and $\epsilon_2(\omega)$) of $\text{Nb}_3\text{O}_7(\text{OH})$ and $\text{H-Nb}_2\text{O}_5$ are calculated.

In Figure 4a, the calculated frequency dependent perpendicular and parallel parts (defined along the crystallographic c -direction) of the imaginary $\epsilon_2(\omega)$ dielectric function are shown for $\text{Nb}_3\text{O}_7(\text{OH})$ and $\text{H-Nb}_2\text{O}_5$. In $\text{Nb}_3\text{O}_7(\text{OH})$, the threshold energy for the perpendicular polarization is 3.19 eV and thus a bit smaller than the energy (3.33 eV) for parallel polarization while the threshold energy for both polarization axes is nearly the same for $\text{H-Nb}_2\text{O}_5$ (3.40 eV).

Furthermore, there are absorption peaks at 3.82/5.16 eV and around 5.81 eV ($\epsilon_2^{\perp}(\omega)$) and 4.53/5.70 eV ($\epsilon_2^{\parallel}(\omega)$) in

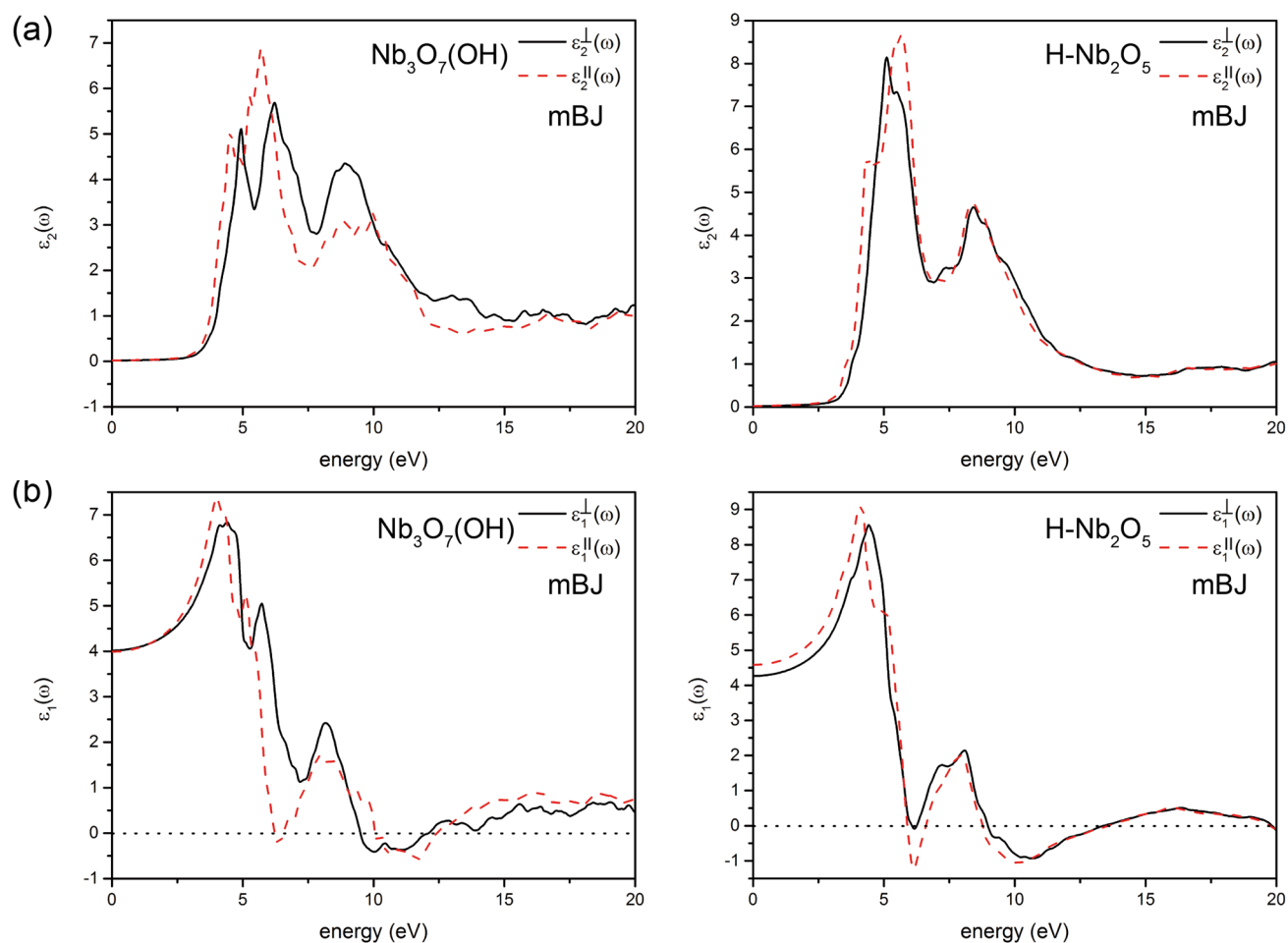


Figure 4. Real and imaginary part of the dielectric function. The peaks result from various transitions. The imaginary $\epsilon_2(\omega)$ and real parts $\epsilon_1(\omega)$ of the DF were calculated for $\text{Nb}_3\text{O}_7(\text{OH})$ and monoclinic $\text{H-Nb}_2\text{O}_5$.

$\text{Nb}_3\text{O}_7(\text{OH})$ which are shifted to 5.83/5.67 eV for $\epsilon_2^\perp(\omega)/\epsilon_2^\parallel(\omega)$ in $\text{H-Nb}_2\text{O}_5$. These peaks are attributed to the allowed transitions of electrons from the VBM (O-2p orbitals) to CBM (Nb-4d orbitals).

Additional absorption peaks are situated at 9.10 eV ($\epsilon_2^\perp(\omega)$) and 10.01 eV ($\epsilon_2^\parallel(\omega)$) in $\text{Nb}_3\text{O}_7(\text{OH})$ and at 8.4 eV for both polarizations in Nb_2O_5 . These peaks result from transitions of electrons from the orbitals below -4.0 eV to orbitals above 4.0 eV. The difference of the absorption peaks observed for $\text{Nb}_3\text{O}_7(\text{OH})$ and Nb_2O_5 is attributed to their different crystal structures.

The calculated real part of the dielectric function, which describes the electronic polarizability of the material, were extracted from the imaginary part of the dielectric function using the Kramers–Kronig expression³⁶ for the perpendicular $\epsilon_1^\perp(\omega)$ and parallel $\epsilon_1^\parallel(\omega)$ polarization (Figure 4b). $\epsilon_1^\perp(\omega)$ shows three maxima at 3.74 eV, 4.72 and 5.54 eV and a smaller feature at 8.08 eV, while $\epsilon_1^\parallel(\omega)$ exhibits two maxima at 4.01 and 5.10 eV for $\text{Nb}_3\text{O}_7(\text{OH})$ and a smaller peaks at 7.98 eV. The spectra of $\text{H-Nb}_2\text{O}_5$ shows one dominant peak at 4.04 eV and one smaller peak at 8.08 eV for $\epsilon_1^\perp(\omega)$ respectively 4.18 and 7.98 eV for $\epsilon_1^\parallel(\omega)$. Both optical components of $\epsilon_1(\omega)$ in $\text{Nb}_3\text{O}_7(\text{OH})/\text{Nb}_2\text{O}_5$ are positive until 9.51/9.24 eV ($\epsilon_1^\perp(\omega)$) and (6.21, 10.05)/(5.89, 8.77)eV ($\epsilon_1^\parallel(\omega)$) and become negative beyond these energies. In addition plasma frequencies are produce at the energy points 11.96 eV/(6.57, 12.45)eV ($\epsilon_1^\perp(\omega)/\epsilon_1^\parallel(\omega)$) in $\text{Nb}_3\text{O}_7(\text{OH})$ and 13.21 eV/(6.63, 13.59

eV) in $\text{H-Nb}_2\text{O}_5$ ($\epsilon_1^\perp(\omega)/\epsilon_1^\parallel(\omega)$) in the positive direction with $\epsilon_1^\perp(\omega)/\epsilon_1^\parallel(\omega) = 0$. The static values of $\text{Nb}_3\text{O}_7(\text{OH})$ are 4.12 eV ($\epsilon_1^\perp(0)$) and 3.98 eV ($\epsilon_1^\parallel(0)$) while $\text{H-Nb}_2\text{O}_5$ is characterized by static values of 4.30 eV ($\epsilon_1^\perp(0)$) and 4.58 eV ($\epsilon_1^\parallel(0)$). This means that $\text{Nb}_3\text{O}_7(\text{OH})$ and $\text{H-Nb}_2\text{O}_5$ obey the Penn model,⁴⁹ which states that larger optical band gaps results in smaller static values.

On the basis of the dielectric function the perpendicular $\sigma^\perp(\omega)$ and parallel $\sigma^\parallel(\omega)$ components of the optical conductivity were calculated for both compounds (Figure 5). There is considerable more optical anisotropy in $\text{Nb}_3\text{O}_7(\text{OH})$ compared to $\text{H-Nb}_2\text{O}_5$ (almost isotropic) for both polarizations. For $\text{Nb}_3\text{O}_7(\text{OH})$, the maximum values of $\sigma^\perp(\omega)$ are situated around 5.83 eV ($4.33 \times 10^{15}\text{s}^{-1}$) and 9.13 eV ($4.25 \times 10^{15}\text{s}^{-1}$) and of $\sigma^\parallel(\omega)$ at 5.73 eV ($4.75 \times 10^{15}\text{s}^{-1}$) and 10.01 eV ($3.95 \times 10^{15}\text{s}^{-1}$). $\text{H-Nb}_2\text{O}_5$ expresses two peaks for both components; for $\sigma^\perp(\omega)$, these peaks are situated at 5.83 eV ($4.44 \times 10^{15}\text{s}^{-1}$) and 8.96 eV ($4.08 \times 10^{15}\text{s}^{-1}$) and for $\sigma^\parallel(\omega)$ at 5.70 eV ($5.96 \times 10^{15}\text{s}^{-1}$) and 8.47 eV ($4.82 \times 10^{15}\text{s}^{-1}$). The difference between the optical conductivity of the two compounds is attributed to their electronic structure as these peaks are mainly composed by the states close to the Fermi level.

III.D. Comparison of the Calculation with Experimental EELS Data. The quality of the calculation was investigated using experimental low loss EEL spectra which were compared to theoretical spectral components of the energy loss function

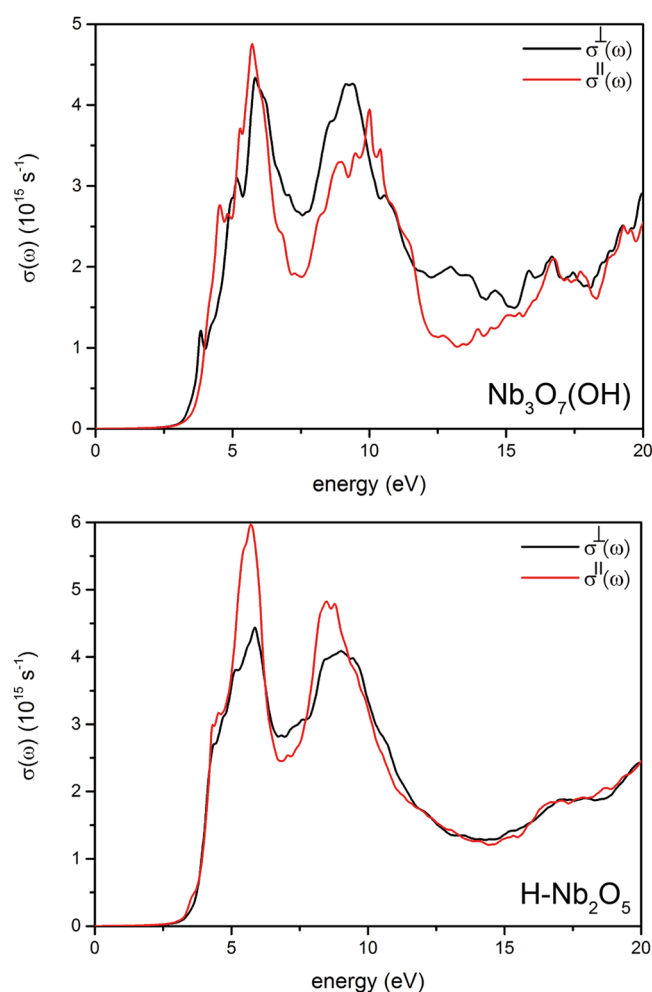


Figure 5. Calculated optical conductivity $\sigma(\omega)$ of $\text{Nb}_3\text{O}_7(\text{OH})$ and monoclinic $\text{H-Nb}_2\text{O}_5$.

$L(\omega)$ for both compounds. Figure 6 shows the spectra $L(\omega)$ which were calculated theoretically using the TB-mBJ functional.³¹ The peaks in $L(\omega)$ have a direct proportionality to the energy loss of fast electrons which transmit through materials. A plasma frequency is produced for the energy points in $\epsilon_1(\omega)$ for which $\epsilon_1^\perp(\omega)/\epsilon_1^\parallel(\omega) = 0$ applies. These are then responsible for the plasmon resonance in $L(\omega)$. Because of the lack of interband transitions the valence shell electrons are regarded as free which results in plasma peaks in both optical spectra of $L^\perp(\omega)/L^\parallel(\omega)$. The low-loss spectra were measured along [100] ($^\perp(\omega)$) and [001] ($^\parallel(\omega)$) direction for $\text{Nb}_3\text{O}_7(\text{OH})$ and off-zone axis for Nb_2O_5 . The experimental spectra for the two crystal directions of $\text{Nb}_3\text{O}_7(\text{OH})$ show broad features at 7 eV and a double peak structure between 12 and 15 eV. The first peak is similar for both crystal directions and can nicely be reproduced by theory which yields a value of 7.1 eV for $L^\perp(\omega)$ and $L^\parallel(\omega)$. The peak intensity of the experimentally observed double peak varies for the two crystal directions: The experimental $L^\parallel(\omega)$ exhibits an enhanced intensity for the first peak at 12 eV, while the second peak at 15 eV is more intense for the experimental $L^\perp(\omega)$. This is also nicely reproduced by theory which exhibits a maximum at 12.47 eV for ($L^\parallel(\omega)$) and 15.0 eV for $L^\perp(\omega)$. The theoretical spectrum $L^\parallel(\omega)$ and $L^\perp(\omega)$ of $\text{H-Nb}_2\text{O}_5$ shows similar features which are positioned at 6.7 and 14.2 eV. Therefore, the experimental spectrum was not acquired along a certain crystal direction. The

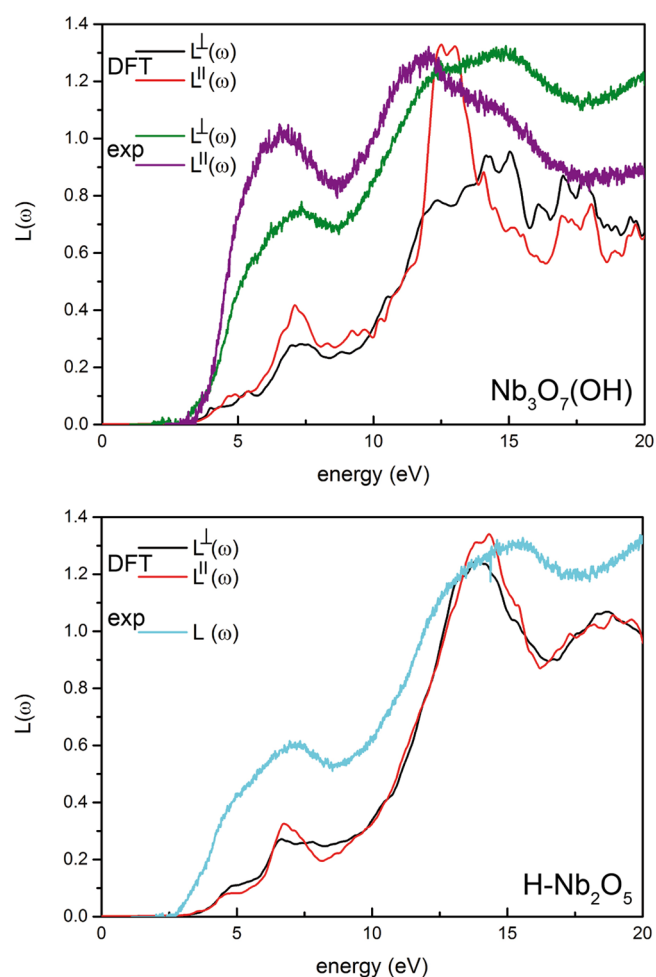


Figure 6. Comparison of the calculated energy loss functions $L(\omega)$ with experimental low loss EEL spectra for $\text{Nb}_3\text{O}_7(\text{OH})$ and $\text{H-Nb}_2\text{O}_5$.

feature observed experimentally resembles the two dominant peaks in the theoretical spectra of $L^\perp(\omega)$ and $L^\parallel(\omega)$.

There is a good agreement between experiment and calculated low-loss features for both compounds, which proves the validity of our structure models. Some finer details of the calculated spectrum could not be resolved experimentally. This might be due to the experimental point spread function which limits the energy resolution.

Element specific electron energy-loss edges give further insights into the local surrounding of the elements in the crystal structure. Both crystal structures $\text{Nb}_3\text{O}_7(\text{OH})$ and monoclinic $\text{H-Nb}_2\text{O}_5$ are composed of edge- and corner-sharing NbO_6 octahedra. This is why no significant differences were observed for the electron energy-loss near edge structure (ELNES) of the experimental Nb-M₃ and O-K edges of the two compounds. In this regard the Nb-M₃ and O-K edge spectra were only calculated for $\text{Nb}_3\text{O}_7(\text{OH})$ to elucidate the contribution of the different lattice sites to the ELNES of the edges. The theoretical spectra were calculated using the WIEN2k code³³ as X-ray absorption spectra (XAS) assuming that EEL spectra are practically the same as XAS spectra for the investigated energy losses. This approximation is valid since the EELS data were acquired within the dipole regime, i.e. small scattering angles. The spectra were obtained as weighted superpositions of spectra generated at each of the inequivalent atomic positions.

Figure 7 summarizes the experimental spectrum, the weighted superposition and the individual contributions of atoms in inequivalent lattice sites.

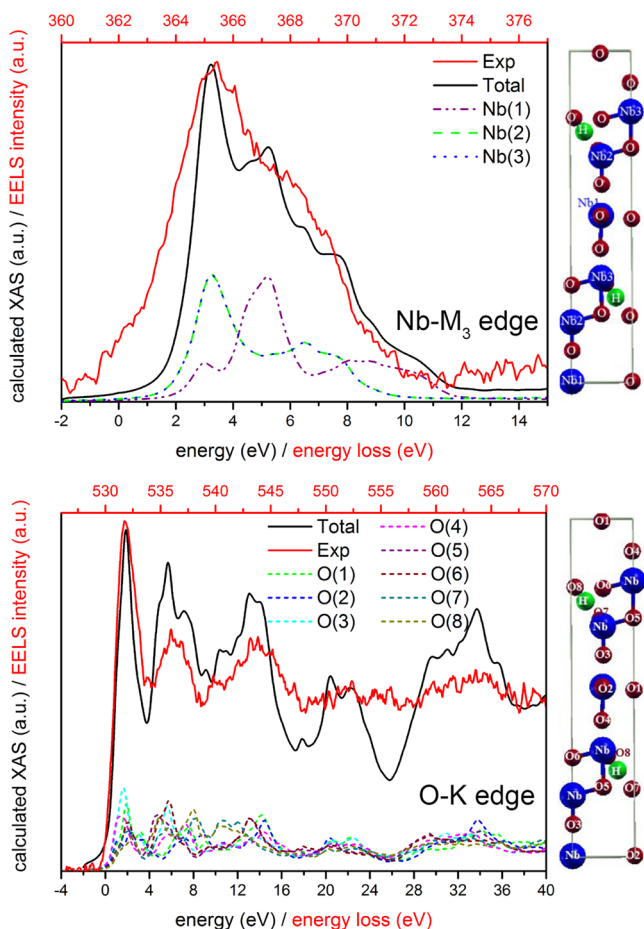


Figure 7. Calculated and measured EELS edges of $\text{Nb}_3\text{O}_7(\text{OH})$. (a) $\text{Nb}-\text{M}_3$ and (b) $\text{O}-\text{K}$ edge.

Pentavalent Nb_2O_5 is characterized by a $\text{Nb}-\text{M}_{2,3}$ edge which exhibits two white lines with high-energy shoulders and is consistent with previously reported ELNES data.⁵⁰ The experimental data of the $\text{Nb}-\text{M}_3$ edge of $\text{Nb}_3\text{O}_5(\text{OH})$ likewise shows one broad line with a maximum at about 3 eV above the onset and a shoulder around 4.2 eV. Our calculations which are based on the dipole selection rule ($\Delta l = \pm 1$)⁵¹ nicely reproduce the ELNES of this edge, which is explained by excitations from the $\text{Nb}-3p_{3/2}$ level to unoccupied $\text{Nb}-4d$ states while dipole allowed transitions from $3p_{3/2}$ to $\text{Nb}-5s$ play a minor role. From the calculations it is obvious that the substructuring of the white line is related to the inequivalent Nb sites in either edge or corner-sharing NbO_6 octahedra. Niobium which sits in the center of edge-sharing NbO_6 octahedra (depicted as Nb(2) and Nb(3) in Figure 7) mainly contributes to the main peak, while the share of the Nb(1) atoms which sit in corner-sharing octahedra dominates the shoulder of the $\text{Nb}-\text{M}_3$ spectrum.

The experimental $\text{O}-\text{K}$ edge, which results from transitions of the $1s$ core electrons to unoccupied states with p character shows five dominant peaks at 2.0, 6.0, 14.0, 22.0, and 33.0 eV above the onset. The entire spectrum could be reproduced nicely by calculations as shown in Figure 7. This was achieved by including the core hole effect into the calculations using the

final state rule. Doing so we performed eight supercell calculations for each inequivalent O-site. The calculations exhibit a huge difference between contributions stemming from different inequivalent oxygen atoms; The first three peaks at 2.0 eV, 6.0 and 13.0 eV at the theoretical scale mainly originates from the following O atoms contributions as follows: (1) the first peak originates from O(1), O(3), and O(4) with minor contribution of O(2, 5–8); (2) the second peak appears mainly due to contributions from O(6) and O(3); (3) the third peak is almost equally contributed by O(6), O(1), and O(3) with minor participation of other O atoms. The remaining two peaks are produced by equal contribution of all O atoms only O(2) participates more at the last peak. Figure 7 shows a nice agreement between the theory and experiment for the $\text{O}-\text{K}$ edge and $\text{Nb}-\text{M}_3$ edge, likewise proving our structure model for $\text{Nb}_3\text{O}_7(\text{OH})$.

III.E. Transport Properties. The electronic transport properties are crucial for the performance of a material in functional devices as electrons and holes need to diffuse through the material subsequent to their generation. These properties are dominated by the effective masses of holes/electrons and their mobilities. The effective masses of electrons and holes were calculated for $\text{Nb}_3\text{O}_7(\text{OH})$ and $\text{H}-\text{Nb}_2\text{O}_5$ by fitting the electronic dispersion curves (E - k curve) around the CBM and VBM niveau:

$$m^* = \hbar^2 \left(\frac{\partial^2 E}{\partial k^2} \right)^{-1} \quad (1)$$

where m^* and \hbar are the effective mass and reduced Planck constant. The calculated effective masses of electrons (m_e^*) are $0.147 m_e$ for $\text{Nb}_3\text{O}_7(\text{OH})$ and $0.112 m_e$ for $\text{H}-\text{Nb}_2\text{O}_5$. Values of $0.351 m_e$ and $0.959 m_e$ were found for the masses of holes (m_h^*) for $\text{Nb}_3\text{O}_7(\text{OH})$ and $\text{H}-\text{Nb}_2\text{O}_5$, respectively. The inverse relation of the effective mass with the mobility of carriers μ_e/μ_h is given by

$$\mu_e = \frac{e\tau}{m_e^*} \text{ and } \mu_h = \frac{e\tau}{m_h^*} \quad (2)$$

with τ being the relaxation time and e the charge of an electron. Accordingly greater effective mass of holes or electrons yield smaller mobilities and vice versa. Both compounds express a higher mobility of electrons resulting in n-type conductivity with $\text{Nb}_3\text{O}_7(\text{OH})$ exceeding $\text{H}-\text{Nb}_2\text{O}_5$.

To elucidate the prospects of $\text{Nb}_3\text{O}_7(\text{OH})$ and $\text{H}-\text{Nb}_2\text{O}_5$ in functional devices the thermoelectric conductivity was calculated under constant relaxation time approximation using the BoltzTraP code.³² In Figure 8, the thermoelectric conductivity σ^{ave} is plotted as a function of the chemical potential μ (eV) at 300 K for both $\text{Nb}_3\text{O}_7(\text{OH})$ and $\text{H}-\text{Nb}_2\text{O}_5$. The $\sigma^{ave}(\mu, T = 300 \text{ K})$ plots are separated into a region below the Fermi level E_F , which is assigned to hole carriers (p-type), and a region above E_F assigned to electrons (n-type). For $\text{Nb}_3\text{O}_7(\text{OH})$, the $\sigma^{ave}(\mu, T = 300 \text{ K})$ plot shows a sharp increase in the n-type region with reaching a value of $1.26 \times 10^{20} (\Omega \text{ ms})^{-1}$ compared to the p-type region ($0.57 \times 10^{20} (\Omega \text{ ms})^{-1}$). The thermoelectric conductivity of $\text{H}-\text{Nb}_2\text{O}_5$ is likewise characterized by a greater value of $3.92 \times 10^{19} (\Omega \text{ ms})^{-1}$ in the n-type region compared to the p-type region were $\sigma^{ave}(\mu, T = 300 \text{ K})$ equals $2.97 \times 10^{19} (\Omega \text{ ms})^{-1}$.

It is worth to note that even though both compounds behaves like n-type semiconductors, the thermoelectric conductivity of electrons is by a factor of 3 higher in

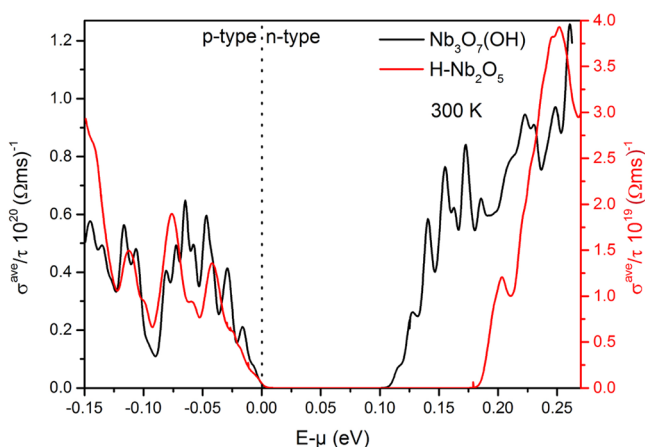


Figure 8. Calculated thermoelectric conductivity for $\text{Nb}_3\text{O}_7(\text{OH})$ (black) and monoclinic $\text{H-Nb}_2\text{O}_5$ (red) calculated using the BoltzTraP code. Please note the different vertical axis values.

$\text{Nb}_3\text{O}_7(\text{OH})$ than in $\text{H-Nb}_2\text{O}_5$. This is in line with the high photochemical efficiency of $\text{Nb}_3\text{O}_7(\text{OH})$ observed experimentally.^{10,24}

IV. CONCLUSION

In summary, we investigated the electronic structure, optical and electronic transport properties of $\text{Nb}_3\text{O}_7(\text{OH})$ and $\text{H-Nb}_2\text{O}_5$ using the TB-mB³¹ functional and developed a model to simulate the presence of hydrogen in the crystal lattice of $\text{Nb}_3\text{O}_7(\text{OH})$. The calculated band structures showed that both compounds are wide and indirect band gap semiconductors, with the calculated optical band gaps being similar to the ones determined experimentally. For both compounds mainly Nb-4d orbitals construct the CBM while O-2p orbitals form the VBM so that transitions between these orbitals are mainly responsible for optical transitions featuring sharp peaks in the dielectric function. Compared to $\text{H-Nb}_2\text{O}_5$, $\text{Nb}_3\text{O}_7(\text{OH})$ shows a greater optical anisotropy and a higher thermoelectric conductivity $\sigma^{\text{ave}}(\mu, T = 300 \text{ K})$. Both compounds express n-type conductivity, and the thermoelectric conductivity of electrons is by a factor three higher in $\text{Nb}_3\text{O}_7(\text{OH})$ compared to $\text{H-Nb}_2\text{O}_5$. Similarly, the thermoelectric conductivity of holes is twice as high in $\text{Nb}_3\text{O}_7(\text{OH})$ than in $\text{H-Nb}_2\text{O}_5$.

Experimental low-loss EEL spectra (energy losses between 0 and 50 eV) were recorded in the TEM for $\text{Nb}_3\text{O}_7(\text{OH})$ and $\text{H-Nb}_2\text{O}_5$. A good agreement between theory and experiment was discovered. These findings validate the results of the calculations and the model for hydrogen positioning. In addition, the WIEN2k code³³ was applied to simulate the ELNES of the Nb-M₃ and O-K edge of $\text{Nb}_3\text{O}_7(\text{OH})$ revealing the contribution of inequivalent lattice sites of the Nb and O atoms.

The results of this study allow an interpretation of the applicability of the two niobium oxide phases orthorhombic $\text{Nb}_3\text{O}_7(\text{OH})$ and monoclinic $\text{H-Nb}_2\text{O}_5$ as photocatalysts or electrode materials. Both compounds exhibit suitable properties but $\text{Nb}_3\text{O}_7(\text{OH})$ exceeds $\text{H-Nb}_2\text{O}_5$ due to higher charge carrier mobility.

■ ASSOCIATED CONTENT

Supporting Information

The Supporting Information is available free of charge on the ACS Publications website at DOI: 10.1021/acs.jpcc.6b06391.

Crystallographic cif files for monoclinic $\text{H-Nb}_2\text{O}_5$ (CIF)
Crystallographic cif files for orthorhombic $\text{Nb}_3\text{O}_7(\text{OH})$ (CIF)

■ AUTHOR INFORMATION

Corresponding Author

*(J.M.) E-mail: jan.minar@cup.uni-muenchen.de. Telephone: +49 (0)89 2180 77589.

Notes

The authors declare no competing financial interest.

■ ACKNOWLEDGMENTS

The theoretical results were developed within the CENTEM project, Reg. No. CZ.1.05/2.1.00/03.0088 and CENTEM PLUS (LO1402). We would like to acknowledge support of supercomputer MetaCenter (LM2010005) and CERIT-SC (CZ.1.05/3.2.00/08.0144). J.M., C.S., and S.B.B. acknowledge support from CeNS, LMU, Munich, and S.B.B. gratefully acknowledges financial support of the “Nanosystems Initiative Munich (NIM)” and for the support of work at the Molecular Foundry by the Office of Science, Office of Basic Energy Sciences, the U.S. Department of Energy under Contract No. DE-AC02-05CH11231. J.M., P.B., and O.S. are supported by COST Action MP1306 EUSpec and W.K. also by the CZ LD15147 of The Ministry of Education, Youth, and Sports.

■ REFERENCES

- Grätzel, M. Dye-sensitized Solar Cells. *J. Photochem. Photobiol., C* **2003**, *4*, 145–153.
- Kudo, A.; Miseki, Y. Heterogeneous Photocatalyst Materials for Water Splitting. *Chem. Soc. Rev.* **2009**, *38*, 253–278.
- Maeda, K.; Domen, K. New Non-Oxide Photocatalysts Designed for Overall Water Splitting under Visible Light. *J. Phys. Chem. C* **2007**, *111*, 7851–7861.
- Cendula, P.; Tilley, S. D.; Gimenez, S.; Bisquert, J.; Schmid, M.; Grätzel, M.; Schumacher, J. O. Calculation of the Energy Band Diagram of a Photoelectrochemical Water Splitting Cell. *J. Phys. Chem. C* **2014**, *118*, 29599–29607.
- Matsumoto, Y. Energy Positions of Oxide Semiconductors and Photocatalysis with Iron Complex Oxides. *J. Solid State Chem.* **1996**, *126*, 227–234.
- Xu, Y.; Schoonen, M. A. A. The Absolute Energy Positions of Conduction and Valence Bands of Selected Semiconducting Minerals. *Am. Mineral.* **2000**, *85*, 543–556.
- Castelli, I. E.; Olsen, T.; Datta, S.; Landis, D. D.; Dahl, S.; Thygesen, K. S.; Jacobsen, K. W. Computational Screening of Perovskite Metal Oxides for Optimal Solar Light Capture. *Energy Environ. Sci.* **2012**, *5*, 5814–5819.
- Yang, L.; Zhou, H.; Fan, T.; Zhang, D. Semiconductor Photocatalysts for Water Oxidation: Current Status and Challenges. *Phys. Chem. Chem. Phys.* **2014**, *16*, 6810–6826.
- Osterloh, F. E. Inorganic Materials as Catalysts for Photochemical Splitting of Water. *Chem. Mater.* **2008**, *20*, 35–54.
- Zhang, H.; Wang, Y.; Yang, D.; Li, Y.; Liu, H.; Liu, P.; Wood, B.; Zhao, H. Directly Hydrothermal Growth of Single Crystal $\text{Nb}_3\text{O}_7(\text{OH})$ Nanorod Film for High Performance Dye-Sensitized Solar Cells. *Adv. Mater.* **2012**, *24*, 1598–1603.
- Rani, R. A.; Zoofakar, A. S.; O’Mullane, A. P.; Austin, M. W.; Kalantar-Zadeh, K. Thin Films and Nanostructures of Niobium Pentoxide: Fundamental Properties, Synthesis Methods and Applications. *J. Mater. Chem. A* **2014**, *2*, 15683–15703.
- Wu, J.; Wang, J.; Li, H.; Xue, D. Solution-Phase Tailored Growth of $\text{Nb}_3\text{O}_7(\text{OH})$ Thin Films. *Thin Solid Films* **2013**, *544*, 545–550.
- Hmadeh, M.; Hoepfner, V.; Larios, E.; Liao, K.; Jia, J.; Jose-Yacamán, M.; Ozin, G. A. New Hydrogen-Evolution Heteronanos-

structured Photocatalysts: Pt-Nb₃O₇(OH) and Cu-Nb₃O₇(OH). *ChemSusChem* **2014**, *7*, 2104–2111.

(14) Betzler, S. B.; Wisnet, A.; Breitbach, B.; Mitterbauer, C.; Weickert, J.; Schmidt-Mende, L.; Scheu, C. Template-Free Synthesis of Novel, Highly-Ordered 3D Hierarchical Nb₃O₇(OH) Superstructures with Semiconductive and Photoactive Properties. *J. Mater. Chem. A* **2014**, *2*, 12005–12013.

(15) Betzler, S. B.; Harzer, T.; Ciston, J.; Dahmen, U.; Dehm, G.; Scheu, C. Heat-Induced Phase Transformation of Three-Dimensional Nb₃O₇(OH) Superstructures: Effect of Atmosphere and Electron Beam. *Cryst. Growth Des.* **2016**, *16*, 4309–4317.

(16) Hu, P.; Hou, D.; Wen, Y.; Shan, B.; Chen, C.; Huang, Y.; Hu, X. Self-Assembled 3D Hierarchical Sheaf-like Nb₃O₇(OH) Nanostructures with Enhanced Photocatalytic Activity. *Nanoscale* **2015**, *7*, 1963–1969.

(17) Sayama, K.; Sugihara, H.; Arakawa, H. Photoelectrochemical Properties of a Porous Nb₂O₅ Electrode Sensitized by a Ruthenium Dye. *Chem. Mater.* **1998**, *10*, 3825–3832.

(18) Prado, A. G. S.; Bolzon, L. B.; Pedroso, C. P.; Moura, A. O.; Costa, L. L. Nb₂O₅ as Efficient and Recyclable Photocatalyst for Indigo Carmine Degradation. *Appl. Catal., B* **2008**, *82*, 219–224.

(19) Ghosh, R.; Brennaman, M. K.; Uher, T.; Ok, M. R.; Samulski, E. T.; McNeil, L. E.; Meyer, T. J.; Lopez, R. Nanoforest Nb₂O₅ Photoanodes for Dye-Sensitized Solar Cells by Pulsed Laser Deposition. *ACS Appl. Mater. Interfaces* **2011**, *3*, 3929–3935.

(20) Lin, H.-Y.; Yang, H.-C.; Wang, W.-L. Synthesis of Mesoporous Nb₂O₅ Photocatalysts with Pt, Au, Cu and NiO Cocatalyst for Water Splitting. *Catal. Today* **2011**, *174*, 106–113.

(21) Ou, J. Z.; Rani, R. A.; Ham, M.-H.; Field, M. R.; Zhang, Y.; Zheng, H.; Reece, P.; Zhuiykov, S.; Sriram, S.; Bhaskaran, M.; et al. Elevated Temperature Anodized Nb₂O₅: A Photoanode Material with Exceptionally Large Photoconversion Efficiencies. *ACS Nano* **2012**, *6*, 4045–4053.

(22) Zhao, Y.; Zhou, X.; Ye, L.; Tsang, S. C. E. Nanostructured Nb₂O₅ Catalysts. *Nano Rev.* **2012**, *3*, 17631–17641.

(23) Cui, H.; Zhu, G.; Xie, Y.; Zhao, W.; Yang, C.; Lin, T.; Gu, H.; Huang, F. Black Nanostructured Nb₂O₅ with Improved Solar Absorption and Enhanced Photoelectrochemical Water Splitting. *J. Mater. Chem. A* **2015**, *3*, 11830–11837.

(24) Zhang, H.; Wang, Y.; Liu, P.; Chou, S. L.; Wang, J. Z.; Liu, H.; Wang, G.; Zhao, H. Highly Ordered Single Crystalline Nanowire Array Assembled Three-Dimensional Nb₃O₇(OH) and Nb₂O₅ Superstructures for Energy Storage and Conversion Applications. *ACS Nano* **2016**, *10*, 507–514.

(25) Parr, R. *Density-Functional Theory of Atoms and Molecules*; International Series of Monographs on Chemistry; Oxford University Press: 1989.

(26) Kohn, W. Nobel Lecture: Electronic Structure of Matter—Wave Functions and Density Functionals. *Rev. Mod. Phys.* **1999**, *71*, 1253–1266.

(27) Perdew, J. P.; Burke, K.; Ernzerhof, M. Generalized Gradient Approximation Made Simple. *Phys. Rev. Lett.* **1996**, *77*, 3865–3868.

(28) Heyd, J.; Peralta, J. E.; Scuseria, G. E.; Martin, R. L. Energy Band Gaps and Lattice Parameters Evaluated with the Heyd-Scuseria-Ernzerhof Screened Hybrid Functional. *J. Chem. Phys.* **2005**, *123*, 174101.

(29) Perdew, J. P.; Wang, Y. Accurate and Simple Analytic Representation of the Electron-Gas Correlation Energy. *Phys. Rev. B: Condens. Matter Mater. Phys.* **1992**, *45*, 13244–13249.

(30) Engel, E.; Vosko, S. H. Exact Exchange-only Potentials and the Virial Relation as Microscopic Criteria for Generalized Gradient Approximations. *Phys. Rev. B: Condens. Matter Mater. Phys.* **1993**, *47*, 13164–13174.

(31) Tran, F.; Blaha, P. Accurate Band Gaps of Semiconductors and Insulators with a Semilocal Exchange-Correlation Potential. *Phys. Rev. Lett.* **2009**, *102*, 226401.

(32) Madsen, G. K.; Singh, D. J. BoltzTraP. A Code for Calculating Band-Structure Dependent Quantities. *Comput. Phys. Commun.* **2006**, *175*, 67–71.

(33) Blaha, P.; Schwarz, K.; Madsen, G.; Kvasnicka, D.; Luitz, J. *WIEN2k: An Augmented Plane Wave plus Local Orbitals Program for Calculating Crystal Properties*; Techn. Universität Wien: Vienna, 2001.

(34) Ambrosch-Draxl, C.; Sofo, J. O. Linear Optical Properties of Solids within the Full-Potential Linearized Augmented Planewave Method. *Comput. Phys. Commun.* **2006**, *175*, 1–14.

(35) Wooten, F. *Optical Properties of Solids*; Academic Press: New York, 1972.

(36) Singh, D. J.; Seo, S. S. A.; Lee, H. N. Optical Properties of Ferroelectric Bi₄Ti₃O₁₂. *Phys. Rev. B: Condens. Matter Mater. Phys.* **2010**, *82*, 180103.

(37) Groh, D.; Pandey, R.; Sahariah, M.; Amzallag, E.; Baraille, I.; R  rat, M. First-Principles Study of the Optical Properties of BeO in its Ambient and High-Pressure Phases. *J. Phys. Chem. Solids* **2009**, *70*, 789–801.

(38) Jorissen, K.; Rehr, J. J. Calculations of Electron Energy Loss and X-ray Absorption Spectra in Periodic Systems without a Supercell. *Phys. Rev. B: Condens. Matter Mater. Phys.* **2010**, *81*, 245124.

(39) Ashcroft, N.; Mermin, N. *Solid State Physics*; HRW International: 1976.

(40) Ziman, J. M. *Principles of the Theory of Solids*, 2nd ed.; Cambridge University Press: 1972; Cambridge Books Online.

(41) Park, J.; Heo, S.; Chung, J.; Kim, H.; Lee, H.; Kim, K.; Park, G. Band Gap Measurement of Thin Dielectric Films using Monochromated STEM-EELS. *Ultramicroscopy* **2009**, *109*, 1183–1188.

(42) Tauc, J.; Grigorovici, R.; Vancu, A. Optical Properties and Electronic Structure of Amorphous Germanium. *Phys. Status Solidi B* **1966**, *15*, 627–637.

(43) Andersson, S.; et al. The Crystal Structure of Nb₃O₇. *Acta Chem. Scand.* **1964**, *18*, 2339–2344.

(44) Izumi, F.; Kodama, H. Hydrothermal Synthesis and Characterization of Nb₃O₇(OH). *Z. Anorg. Allg. Chem.* **1978**, *441*, 196–204.

(45) Betzler, S. 3D Hierarchical Nb₃O₇(OH) Superstructures: Synthesis, Structural Characterization and Photophysical Properties. Ph.D. Thesis, Faculty of Chemistry and Pharmacy, Ludwig-Maximilians-University of Munich: Munich, 2015.

(46) Gatehouse, B.; Wadsley, A. The Crystal Structure of the High Temperature Form of Niobium Pentoxide. *Acta Crystallogr.* **1964**, *17*, 1545–1554.

(47) Kato, K. Structure Refinement of H-Nb₂O₅. *Acta Crystallogr., Sect. B: Struct. Crystallogr. Cryst. Chem.* **1976**, *32*, 764–767.

(48) Scanlon, D. O.; Dunnill, C. W.; Buckeridge, J.; Shevlin, S. A.; Logsdail, A. J.; Woodley, S. M.; Catlow, R. A.; Powell, M. J.; Palgrave, R. G.; Parkin, I. P.; et al. Band Alignment of Rutile and Anatase TiO₂. *Nat. Mater.* **2013**, *12*, 798–801.

(49) Penn, D. R. Wave-Number-Dependent Dielectric Function of Semiconductors. *Phys. Rev.* **1962**, *128*, 2093–2097.

(50) Bach, D.; Schneider, R.; Gerthsen, D.; Verbeeck, J.; Sigle, W. EELS of Niobium and Stoichiometric Niobium-Oxide Phase Part I: Plasmons and Near-Edge Fine Structures. *Microsc. Microanal.* **2009**, *15*, 505–523.

(51) Rubio, M.; Serrano-Andres, L.; Merch  n, M. Excited States of the Water Molecule: Analysis of the Valence and Rydberg Character. *J. Chem. Phys.* **2008**, *128*, 104305–104317.